Article

NMR of Paramagnetic Proteins: ^{13}C Derived Paramagnetic Relaxation Enhancements Are an Additional Source of Structural Information in Solution

Leonardo Querci [1], Inês B. Trindade [2], Michele Invernici [1], José Malanho Silva [1], Francesca Cantini [1], Ricardo O. Louro [2,*] and Mario Piccioli [1,*]

[1] Magnetic Resonance Center and Department of Chemistry, University of Florence, Via L. Sacconi 6, 50019 Sesto Fiorentino, Italy
[2] Instituto de Tecnologia Química e Biológica António Xavier (ITQB-NOVA), Universidade Nova de Lisboa, Av. da República (EAN), 2780-157 Oeiras, Portugal
* Correspondence: louro@itqb.unl.pt (R.O.L.); piccioli@cerm.unifi.it (M.P.); Tel.: +351-214469332 (R.O.L.); +39-055-4574188 (M.P.)

Abstract: In paramagnetic metalloproteins, longitudinal relaxation rates of ^{13}C′ and ^{13}C$^\alpha$ nuclei can be measured using ^{13}C detected experiments and converted into electron spin-nuclear spin distance restraints, also known as Paramagnetic Relaxation Enhancement (PRE) restraints. ^{13}C are less sensitive to paramagnetism than ^{1}H nuclei, therefore, ^{13}C based PREs constitute an additional, non-redundant, structural information. We will discuss the complementarity of ^{13}C PRE restraints with ^{1}H PRE restraints in the case of the High Potential Iron Sulfur Protein (HiPIP) PioC, for which the NMR structure of PioC has been already solved by a combination of classical and paramagnetism-based restraints. We will show here that ^{13}C R_1 values can be measured also at very short distances from the paramagnetic center and that the obtained set of ^{13}C based restraints can be added to ^{1}H PREs and to other classical and paramagnetism based NMR restraints to improve quality and quantity of the NMR information.

Keywords: HIPIP; iron-sulfur proteins; metalloproteins; structural biology; paramagnetic NMR; paramagnetic relaxation enhancement; NMR solution structure

1. Introduction

Metalloproteins play crucial roles in catalysis, electron transfer, metal storage/transport. Many of them are available in two different oxidation states and are paramagnetic in at least one of them [1,2]. NMR can provide the structure in solution at atomic resolution of paramagnetic proteins [3]. Tailored NMR experiments, paramagnetism-based structural restraints, and ad-hoc structure calculation programs allowed obtaining solution structures of paramagnetic proteins with a resolution comparable, if not better, with that of diamagnetic analogues of similar size [4–12]. In this scenario, relaxation-based NMR restraints are a powerful class of dipole–dipole restraints, providing through-space connectivities between the NMR active nuclei and the metal center(s) [13–23]. We have shown that, when a sufficient number of Paramagnetic Relaxation Enhancements (PRE, hereafter) effects are measurable throughout the entire protein, PREs restrain the conformational space with an efficiency comparable to Nuclear Overhauser Effects (NOE), even though they originate a set of distances all involving a single point, i.e., the paramagnetic center [24]. In the case of the NMR structure of the small paramagnetic protein PioC [25], obtained with a combination of NOE and paramagnetism-based NMR restraints, we showed that the solution structure obtained with only Paramagnetic NMR restraints is essentially the same as the one obtained with the full set of NMR restraints [24]. However, the only PREs used for structure calculations were R_1 and R_2 relaxation rates of ^{1}H spins obtained via ^{13}C- and

[15]N- Heteronuclear Single Quantum Coherences (HSQC) type experiments [26,27]. In order to sample the backbone more accurately, the relaxation rates of $^{13}C'$ and $^{13}C^{\alpha}$ spins are expected to have two advantages: (i) together with H_N and H_{α}, $^{13}C'$ and $^{13}C^{\alpha}$ would provide a set of relaxation rates capable to define the relative orientation of the backbone of each aminoacid with respect to the metal center (Figure 1); (ii) because paramagnetic relaxation depends on γ^2 of the investigated nucleus, ^{13}C are less sensitive to paramagnetism and, therefore, they are expected to provide complementary information with respect to the ^{1}H based PREs: when paramagnetism is strong and ^{1}H signals are not observable, ^{13}C signals are still detectable [28], therefore ^{13}C based PREs constitute an additional, non-redundant, structural information.
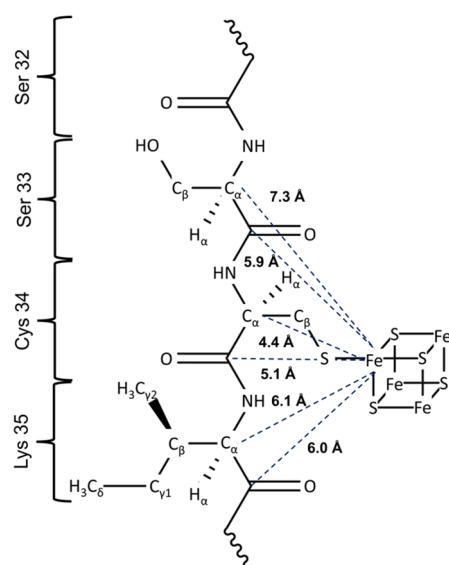

Figure 1. Schematic drawing of protein backbone vs. a metal ion: the availability of a larger number of R_1 values contributes to place the backbone with respect to the metal. The C' and C^{α} distances from the iron ion are reported.

We will test this idea on the protein PioC, that we have already used to study the effects of PREs vs. classical restraints. The Iron-sulfur High Potential Iron Protein (HiPIP) PioC from *Rhodopseudomonas palustris* TIE-1 [25] contains a $[Fe_4S_4]^{3+/2+}$ cluster, being stable in the reduced $[Fe_4S_4]^{2+}$ form. The protein has only 54 amino acids and it is an excellent case to validate novel NMR approaches for paramagnetic molecules. Most of the protein is affected by paramagnetism, but the intensive study by NMR has provided an almost complete sequence-specific assignment and the blind sphere, i.e., the region of the protein where, in principle, no information can be obtained by NMR due to paramagnetic induced line broadening, has been essentially eliminated, opening the way to new approaches of investigation. The methods validated using PioC could then be applied in more challenging systems, in which the paramagnetic relaxation prevents the identification of signals in a large sphere around the metal center [29]. Here, ^{13}C direct detection and ^{13}C PREs may become a precious tool to refine the structure in the proximity of the metal center [30–36]. Towards this aim, here we present how ^{13}C R_1 relaxation rates can be measured using ^{13}C detected experiments in highly paramagnetic systems, further discussing their complementarity and consistency with ^{1}H PRE restraints. Finally, we will consider how the NMR structure of PioC can be refined when ^{13}C based NMR restraints are added into structure calculations.

2. Materials and Methods

Sample preparation. PioC was expressed and purified, as previously reported [25]. Uniformly ^{15}N, ^{13}C labelled PioC was expressed and purified in the M9 minimal media

with the addition of ammonium sulfate ($^{15}N_2$, 99%) and [U-$^{13}C_6$] D-glucose in the M9 minimal media when labelling was required. The detailed procedure has been previously reported [24,37].

R_1 longitudinal relaxation rates of $^{13}C'$ spins. A Bruker Avance III 700 MHz spectrometer operating at 700.06 MHz ^{1}H frequency, equipped with a 5 mm, cryogenically cooled, inverse detection probe head (TXI), was used to measure $^{13}C'$ R_1 longitudinal relaxation rates. Two series of HNCO-T_1 experiments were recorded with parameters summarized in Table 1. The series with 7 s of recycle delay was recorded using the following relaxation delays: 2 ms, 50 ms, 150 ms, 200 ms, 400 ms, 600 ms, 1 s, 1.5 s, 2 s, 3 s and 5 s. The series recorded with 2 s of recycle delay, the relaxation delays were: 2 ms, 6 ms, 10 ms, 16 ms, 24 ms, 50 ms, 70 ms, 100 ms, 140 ms, 220 ms, 350 ms, 360 ms, 500 ms and 700 ms. R_1 of fast relaxing C' spins were measured using a tailored IR-COCA-AP. Experiments were recorded at 700 MHz Bruker AVANCE NEO spectrometer, equipped with a 5 mm cryogenically cooled probe head optimized for ^{13}C direct detection (CT-TXO), operating at 176.05 MHz ^{13}C frequency. The $^{13}C'$-C$^\alpha$ evolution delay was set to 2.7 ms, the IPAP scheme for virtual homonuclear decoupling was abolished, acquisition and recycle delays were shortened (see Table 1) to increase the number of transients per experimental time. The inversion recovery delays were: 1 ms, 10 ms, 50 ms, 80 ms, 120 ms, 200 ms, 300 ms, 500 ms, 800 ms, 1.2 s and 2 s. Longitudinal relaxation rates of carbonyl spins of Proline preceding residues were measured using a CON-T_1 experiment (Table 1) with the following delays for the inversion recovery of the magnetization: 2 ms, 50 ms, 100 ms, 150 ms, 200 ms, 400 ms, 600 ms, 1 s, 1.5 s, 2 s, 3.5 s and 5 s.

Table 1. Experiments performed and relevant parameters.

Experiment	Time Domain		Number of Scan	Spectral Width (ppm)		Acquisition Time (ms)		Recycle Delay (s)
	F2	F1		F2	F1	F2	F1	
HNCO-T_1	1024	64	16	13.7	36	53	12.5	7
HNCO-T_1	1024	96	64	13.7	50	53	12.5	2
CON-T_1	1024	96	32	40.6	51	71.7	13.3	6.4
IR-COCA-AP	1024	128	48	64.5	25	45	14.5	2
IR-COCA-AP *	512	96	192	40.6	40	35.8	6.8	1
IR-CACO-IPAP	512	64	16	31.6	30	46	6	5
IR-CACO-AP	512	128	32	31.6	30	46	12.1	2
IR-CACO-AP *	512	96	224	31.6	50	46	5.4	0.5

* Series of experiments to measure Cysteines C'/C$^\alpha$ longitudinal relaxation rates.

R_1 longitudinal relaxation rates $^{13}C^\alpha$ spins. C$^\alpha$ nuclei longitudinal relaxation rates measurements were recorded at a 700 MHz NMR spectrometer, equipped with a probe head optimized for ^{13}C direct detection experiments, as mentioned above. A series of experiments was collected using a IR-CACO-IPAP pulse sequence [38] in which the inversion recovery delays were: 5 ms, 100 ms, 220 ms, 340 ms, 460 ms, 700 ms, 1 s, 1.6 s, 2.4 s, 3.6 s, 4.6 s and 5 s. An IR-CACO-AP series was recorded to sample fast relaxing C$^\alpha$ spins. The experiment is optimized as described above (Table 1). The inversion recovery delays used were: 1 ms, 5 ms, 10 ms, 20 ms, 40 ms, 60 ms, 80 ms, 120 ms, 200 ms, 300 ms, 500 ms, 800 ms, 1.2 s and 2 s. All the experiments were recorded using waltz65 and garp4 decoupling scheme for ^{1}H and ^{15}N decoupling. Smoothed square shape for all gradients was used. Q5- and Q3-shaped pulses, with a duration of 300 and 231 μs respectively, [39] were used for ^{13}C band-selective $\pi/2$ and π flip angle pulses.

Data analysis and assessment. All the spectra were processed with a squared cosine weighting functions on Topspin 4.0.8 software. Exponential decays of the inversion recovery experiments were evaluated using cross-peak intensities. The intensity of each signal was integrated using Computed Aided Resonance Assignment (CARA) software [40]. All relaxation data were analyzed using the Origin 2022 software (v9.9.5). Peak intensities were fitted with a three-parameter exponential decay model.

Structure calculation. Structure calculations were performed with the software CYANA 2.1 [41–43]. NOEs converted into upper distance limits, backbone dihedral angle constraints and ^{1}H PREs restraints were derived from the previously calculated and deposited structure (PDB: 6XYV) [24]. In the final structure calculation, 2000 conformers are calculated using the standard simulated annealing schedule with 65,000 torsion angle dynamics steps per conformer. The 20 conformers with the lowest Target Function are analyzed and compared with the previous deposited structure that was calculated with the same procedure. Details about the FeS cluster design and insertion into the structure calculation were previously reported [24].

3. Results and Discussion

3.1. Measurements of $^{13}C'$ Longitudinal Relaxation Rates via ^1H Detection Methods

$^{13}C'$ longitudinal relaxation rates can be collected via an HNCO-type experiment [44]. The experiment gives rise to an HSQC-type spectrum in which the signal intensity of each H_i-N_i peak is modulated by the R_1 relaxation rate of the preceding carbonyl (C'_{i-1}). Proton magnetization is decoupled during the inversion recovery of $^{13}C'$ spins, while no inversion pulses are given on $^{13}C^\alpha$ and ^{15}N. This sequence does not remove cross correlation effects between $^{13}C'_z$ with both $^{13}C^\alpha$ and ^{15}N, which may be operative during the longitudinal recovery delay of $^{13}C'$ spins. In order to properly sample the decay of both fast and slow relaxing signals, the experiment was, indeed, repeated twice with two different set of recovery and recycle delays. Obtained results are summarized in Table 2.

Table 2. R_1 measured for C' and C^α nuclei and related upper limit restraint used in structure calculation.

Residues		Exp	$R_1 C'$ (s^{-1})	Err	Upl (C'-ME)	Residues		Exp	$R_1 C\alpha$ (s^{-1})	Err	Upl (C$^\alpha$-ME)
VAL	1	*	1.19	0.1		VAL	1	~	2.09	0.5	
THR	2					THR	2				
LYS	3					LYS	3				
LYS	4					LYS	4				
ALA	5	*	1.06	0.1		ALA	5	~	1.76	0.1	
SER	6	*	1.23	0.4		SER	6	~	1.84	0.4	
HIS	7					HIS	7	~	1.78	0.1	
LYS	8	*	1.14	0.2		LYS	8				
ASP	9	*	1.06	0.1		ASP	9	~	1.79	0.1	
ALA	10	*	1.55	0.1	8.02	ALA	10	~	2.31	0.2	
GLY	11	*	1.43	0.1	8.43	GLY	11	~	3.61	0.3	
TYR	12	*	1.42	0.1	8.46	TYR	12	~	3.12	0.3	6.82
GLN	13	*	1.26	0.1		GLN	13	~	2.37	0.2	
GLU	14	*	0.88	0		GLU	14	~	1.79	0.1	
SER	15	¬	2.11	1.5		SER	15	~	1.85	0.5	
PRO	16	*	1.05	0.1		PRO	16	~	1.87	0.2	
ASN	17	*	1.08	0.1		ASN	17	~	2.04	0.2	
GLY	18	*	0.93	0.1		GLY	18	~	3.25	0.4	
ALA	19	*	1.24	0.8		ALA	19	~	1.57	0.1	
LYS	20					LYS	20				
ARG	21					ARG	21				
CYS	22	##	5.96	0.9	6.11	CYS	22	>	18.32	1.7	5.72
GLY	23	*	1.26	0.1	9.59	GLY	23	~	3.37	0.2	
THR	24	**	5.87	2.2		THR	24	~~	2.19	0.4	
CYS	25	##	4.93	0.7	6.32	CYS	25	>	14.1	1.9	5.93
ARG	26					ARG	26				
GLN	27	#	7.68	1	5.56	GLN	27	~~	7.07	0.6	
PHE	28	*	2.07	1.4	7.16	PHE	28	~~	8.82	1.1	5.51

Table 2. *Cont.*

Residues		Exp	R₁ C′ (s⁻¹)	Err	Upl (C′-ME)	Residues		Exp	R₁ Cα (s⁻¹)	Err	Upl (Cα-ME)
ARG	29					ARG	29				
PRO	30	¬	1.47	1.2		PRO	30	~	1.65	0.2	
PRO	31	*	1.11	0.1		PRO	31	~	1.41	0.1	
SER	32	*	1.19	0.1		SER	32				
SER	33	**	4.55	0.9		SER	33	~	1.95	0.3	9.17
CYS	34	##	3.53	0.5	6.75	CYS	34	>	13.44	0.8	5.97
ILE	35					ILE	35	~	2.12	0.5	8.26
THR	36					THR	36	~~	4.35	0.9	
VAL	37	**	4.34	0.4		VAL	37	~~	4.93	0.4	
GLU	38	*	1.28	0.1	9.35	GLU	38	~	2.15	0.1	
SER	39	¬	1.45	1.1		SER	39	~	2.32	0.5	
PRO	40	*	1.18	0.1		PRO	40	~	1.83	0.2	
ILE	41	*	1.63	0.2	7.82	ILE	41	~	2.56	0.6	7.34
SER	42	*	1.86	0.1		SER	42	~	3.51	0.5	
GLU	43	*	1.55	0.1	8.04	GLU	43	~	2.28	0.2	
ASN	44	*	1.56	0.1	8	ASN	44	~	1.68	0.2	
GLY	45	#	4.56	0.6	6.04	GLY	45	~~	4.42	0.4	
TRP	46	#	8.79	1	5.45	TRP	46	~~	9.58	1.7	5.44
CYS	47	##	8.54	1.5	5.78	CYS	47	>	18.58	4.3	7.71
ARG	48					ARG	48				
LEU	49					LEU	49				
TYR	50					TYR	50	~	3.07	1.4	6.86
ALA	51	*	2.03	0.1		ALA	51	~	2.94	0.2	
GLY	52					GLY	52	~	3.22	0.3	
LYS	53	*	1.31	0.5		LYS	53				
ALA	54					ALA	54				

Experiment are associated with each symbol as follows: * HNCO-T_1 (Slow), ** HNCO-T_1 (Fast), ¬ CON-T_1, # IR-COCA-AP, ## IR-COCA-AP*, ~ IR-CACO-IPAP, ~~ IR-CACO-AP, > IR-CACO-AP*.

In our hands, the HNCO-T_1 experiment was hardly susceptible to experimental optimization with respect to fast relaxing signals. The in-phase carbonyl single quantum coherence is created via a refocused N-C′ INEPT step which requires, for the out-and-back pathway, about 100 ms. A refocused INEPT cannot be significantly shortened without losing the efficiency of the transfer and, consequently, the formation C′$_z$ signal is in phase. Accordingly, many R_1 values cannot be properly measured due to efficient paramagnetic relaxation effective during the HNCO block.

3.2. Measurements of ^{13}C′ Relaxation Rates via ^{13}C Detection Methods

Paramagnetic relaxation depends on γ^2 of the relaxing nucleus, therefore the use of "protonless" experiments in which ^{1}H spins are decoupled throughout the entire sequence, offers the opportunity to design experiments that are more robust than ^{1}H detected experiments to the loss of information due to paramagnetic relaxation. A CON-T_1 experiment can be easily implemented [45] to obtain ^{13}C R_1 measurements by simply adding an inversion recovery filter prior to the conventional CON sequence. We have used this approach to measure R_1 values of Proline preceding residues, which were obviously missing in the HNCO-T_1 (Table 2). *Vis-à-vis* the optimization for paramagnetic relaxation, we have already shown that a paramagnetically tailored CON experiment allows one to obtain signals from residues closer to the metal than a standard CON [46,47]; however, when one aims at monitoring signals that do not "survive" the long coherence transfer periods, C′/N transfer should be replaced by a C′/Cα transfer. To obtain reliable R_1 measurements in the presence of efficient paramagnetic relaxation effects, we propose the pulse sequence shown in Figure 2a. The experiment is essentially an IR-COCA-AP experiment: the inversion recovery building block for C′ spins will modulate the intensity of a COCA-AP experiment,

in which the C^α is detected in antiphase mode to avoid paramagnetic relaxation during the IPAP block [48]. The spectrum is reported in Figure 3a. This is the shortest and simplest experiment, and the only coherence transfer step can be optimized depending on the relaxation properties of the $C'_y C^\alpha_z$ antiphase magnetization, as shown in Figure 2c. With this experiment we obtained a new set of R_1 C' measurements, that also contained signals unobserved (or measured with a very low precision) in HNCO-T_1 and CON-T_1. In our hands we found that, for R_1 rates larger than 4–5 s^{-1}, the IR-COCA-AP experiment was the most reliable experiment for C' R_1 measurements.
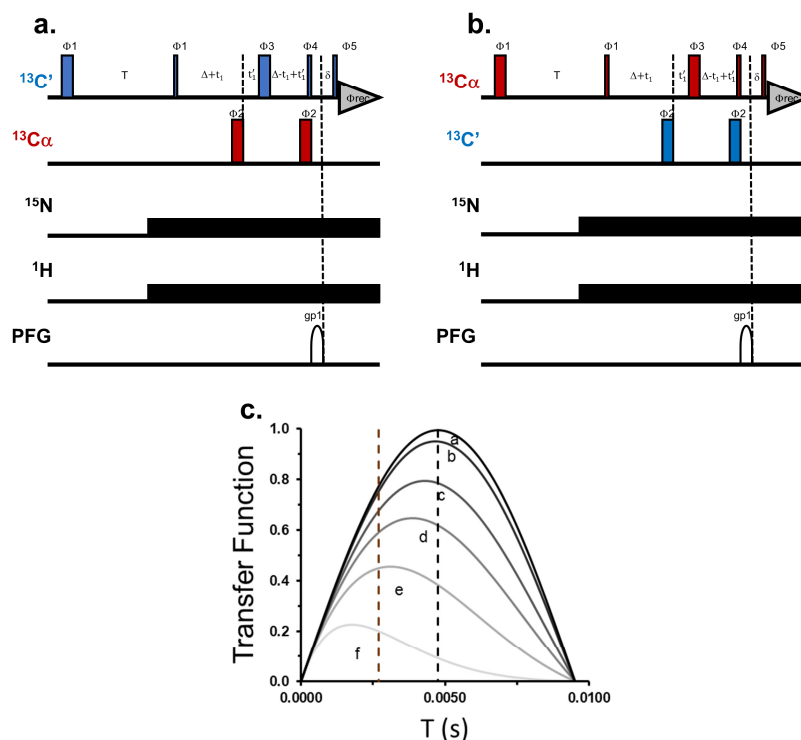
Figure 2. (**a**) IR-COCA-AP; (**b**) IR-CACO-AP Phases as follows: ϕ_1: x,-x; ϕ_2: x; ϕ_3: x,x,x,x, y,y,y,y; ϕ_4: y; ϕ_5: x,x,-x,-x; ϕ_{rec} x,-x,-x,x, -x,x,x,-x. Semi-constant time evolution is given in the indirect dimension. 90° and 180° pulses are given as Q5 and Q3 band selective pulses, respectively. (**c**): calculated efficiency of the coherence transfer function for a C'/C^α coupling (53 Hz) versus the INEPT transfer delay under the effect of relaxation. (a: no relaxation; b: 10 s^{-1}, c: 50 s^{-1}, d: 100 s^{-1}, e: 200 s^{-1}, f: 500 s^{-1}). Black dashed line indicates the delay typically used in the experiment (4.7 ms), red dashed line indicates the delay that we have used throughout the experiments reported in this article (2.7 ms).

3.3. Measurements of $^{13}C^\alpha$ Relaxation Rates via ^{13}C Detection Methods

By swapping the frequencies of C' and C^α, the IR-COCA-AP experiment becomes an IR-CACO-AP experiment, as shown in Figure 2b, where the peak intensity is modulated by $^{13}C^\alpha$ R_1 values. The obtained spectrum is reported in Figure 3b. The evolution delay Δ of the experiment is optimized according to the relaxation properties of the $C^\alpha_y C'_z$ coherence. The effect of paramagnetic relaxation on the coherence transfer function C'/C^α is described by the same function shown in Figure 2c, however the relaxation rates of $C'_y C^\alpha_z$ and the $C^\alpha_y C'_z$ are not the same. Many variants of the CACO experiments have been described in the literature [36]. The CACO-AP that we used here has been widely shown to be the most efficient experiment in the presence of strong paramagnetic relaxation effects [48]. As a proof of concept of the validity of the ^{13}C detected approach, we decided to use here a standard IR-CACO-IPAP [38] to measure relaxation rates of "slow" relaxation $^{13}C^\alpha$ nuclei and the IR-CACO-AP to obtain $^{13}C^\alpha$ R_1 values of fast relaxing signals. The combined approach provided R_1 C^α values in the range 1.5–20 s^{-1}, as summarized in Table 2.
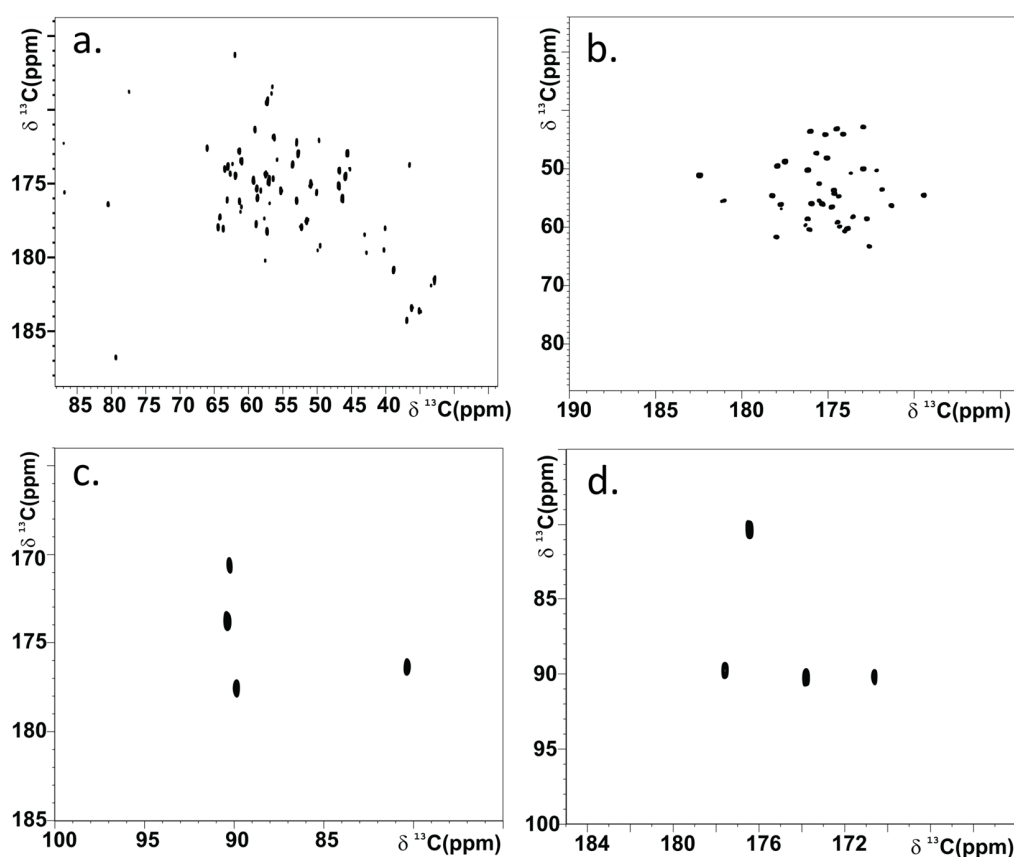
Figure 3. (**a**) IR-COCA-AP spectra; (**b**) IR-CACO-AP (**c**) IR-COCA-AP spectra Cys region; (**d**) IR-CACO-AP Cys region. The reported spectra were recorded using parameters summarized in Table 1. For each R_1 series, the experiment with the longest recovery delay is shown.

3.4. Relaxation Measurements of ^{13}C of Fe-Bound Cysteine Residues

The delocalization of unpaired electron spin density from each iron ion onto the ligands induces significant contact hyperfine shifts on ^{13}C spins of Cys residues. As the main mechanism for this delocalization is the Fe-S- C^{α}- C^{α}-C' sigma bond pathway, the hyperfine shift values of Cys ^{13}C spins are expected to follow this order. For Cysteine residues bound to a $[Fe_4S_4]^{2+}$ cluster we observe, on average, 60–80 ppm, for C^{α}, 30–35 ppm for C^{α} and negligible contributions for C' [49,50]. In order to measure Cys ^{13}C R_1 rates, we set the C^{α} carrier at ca 86 ppm and repeated the experiments discussed above. The four C^{α}/C' connectivities are clearly observed, as shown in Figure 3c,d. As expected, the R_1 rates of Cysteine C' and C^{α} signals, also reported in Table 2, experience the largest ^{13}C PRE values throughout the protein backbone.

3.5. Conversion of Relaxation Rates into Distance Restraints

R_1 values summarized in Table 2 can be factorized according to (1):

$$R_{\text{obs}} = R_{\text{dia}} + R_{\text{para}}, \tag{1}$$

where R_{obs} is the experimentally measured longitudinal relaxation rate, R_{para} is given by the contributions arising from the hyperfine interaction and R_{dia} accounts from all the other contributions to longitudinal relaxation. The ideal strategy to obtain R_{para} contributions would be that of measuring R_{dia} by repeating the experiment on the same sample in a diamagnetic state. Unfortunately, in PioC both oxidation states of $[Fe_4S_4]^{3+/2+}$ are paramagnetic, and the cluster cannot be removed without substantially the structure of the protein. Thus, to factorize the R_{para} contributions, for each series of experiments, the average of R_{obs} values of residues 5–7, that are far from the paramagnetic center, provided

an average value for R_{dia}; that was used in Equation (1) to obtain a list of R_{para} values. This is an approximation because several factors, such as internal mobility, chemical shift anisotropy relaxation and cross correlations, modulate the R_{dia} value of each aminoacid. In turn, R_{para} arises from the sum of electron–nucleus dipole–dipole coupling and unpaired electron delocalization onto the investigated nucleus, the so-called Fermi Contact relaxation Equation (2):

$$R_{\mathrm{para}} = R_{\mathrm{DD}} + R_{\mathrm{FC}}, \tag{2}$$

The first contribution has a r^{-6} dependence from the electron spin (S)—nuclear spin (I) distance, and therefore the contact contribution in principle needs to be factorized out [51]. However, The R_{FC} contact contribution is significant only for Fe-bound Cysteine nuclei, which has been treated separately. All other R_{para} were then directly converted into upper limit distances according to Equation (3):

$$UPL_{\mathrm{ME}} = \left(\frac{K}{R_{\mathrm{par}}} \right)^{\frac{1}{6}} + 1.4 \,, \tag{3}$$

The $\left(\frac{K}{R_{\mathrm{para}}} \right)^{\frac{1}{6}}$ term converts R_{para} into a distance from an iron ion of the cluster, assuming the unpaired spin density in the cluster is localized on the iron ions and that, for each R_{para}, the effect is fully due to the distance from the closest iron ion. To minimize errors due to these approximations, and in order not to be biased from any structural model, each nuclear spin is not restrained to a specific iron of the cluster but to the center of the mass of the cubane (ME), which is located at about 1.4 Å from the edges of the cubane where iron ions are located. The UPL_{ME} used in the structure calculation are also reported in Table 2. Concerning the eight restraints from $^{13}C^{\alpha}$ and $^{13}C'$ of cluster bound Cys residues, we used the same approach used for the other R_{para} values, and then we empirically applied a tolerance to remove the consistent violations on these distances. We obtained structure with acceptable target functions by increasing the calculated distance of C^{α} and C' by 15% and 5%, respectively.

3.6. Structure Calculations

^{13}C derived PREs were included in the structure calculation to refine the NMR structure of PioC and to assess the efficiency of these constraints. The 27 C' and C^{α} constraints were added to the structure restraints available [52–54] for this protein, that are summarized in Table 3. The structure obtained with this extended set of NMR restraints is shown in Figure 4, together with the structure obtained without ^{13}C PREs. Within the uncertainty, the pairwise RMSD to the mean of the structure obtained with the new set of restraints is the same as the one obtained previously. The backbone RMSD between the mean structures of the two families is 0.43 Å. This compares with the backbone RMSD values of 0.46 ± 0.11 Å and 0.43 ± 0.10 Å, observed for the families with and without ^{13}C PREs, thus indicating that the two structures are identical. Figure 5 shows that, with the exception of a small region between Cys25 and Cys 34, the per-residue RMSD between the two average structures is always lower than the sum of the RMSD of the two families [55]. This means that the two structures are distinguishable only for a small rearrangement in the residues 27–28, which correspond to the protein region following Cys25, while no significant variations are observed for the rest of the protein structure. The small increase in target function (Table 3) indicates that the new set of restraints is fully compatible with the previous one and contribute to finding a convergent energy minimum. Figure 6 shows the ^{13}C PRE-based distance restraints obtained here vs. the ensemble of conformers with and without their use in the structure calculations. ^{13}C PRE-based restraints are fully congruent and integrated into the full set of NMR restraints. The addition of ^{13}C restraints results in a lower dispersion of the calculated distances, particularly relevant for residues located in the 5–9 Å sphere from the cluster. The plot also shows that Tyrosine 50 retains a high

divergence, due to the fact that very few restraints are available for this residue, which the new set of ^{13}C restraints was not able to reduce.

Table 3. The table summarizes the structural restraints utilized in ensemble calculations and the results derived from PSVS (v1.5) analysis performed on the obtained family structures.

	Full Set	^{13}C *PRE-Less Restraints*
Total number of meaningful NOE upper distance constraints:	344	344
Total meaningful dihedral angle restraints:	51	51
Total number of paramagnetic NMR restraints:	216	189
Residual CYANA Target Function:	1.47 ± 0.06	1.07 ± 0.08
Pairwise RMSD to the mean:		
Backbone RMSD$ (residues 5–50):	0.46 ± 0.07	0.43 ± 0.10
All heavy at.RMSD$ (residues 5–50):	1.03 ± * 0.23	1.14 ± 0.16
*Ramachandran Plot Summary from Procheck *:*		
Most favored regions:	63.70%	65.50%
Additionally allowed regions:	34.60%	32.80%
Generously allowed regions:	1.70%	1.40%
Disallowed regions:	0.00%	0.30%
Average no. of distance viol/stru:		
>0.5 Å:	0	0
RMS of Distances violations per meaningful distance constraint (Å):	0.0204	0.0146

* Selected residue ranges: 5–50. Calculated using PSVS 1.5 (Bhattacharya et al. 2007).
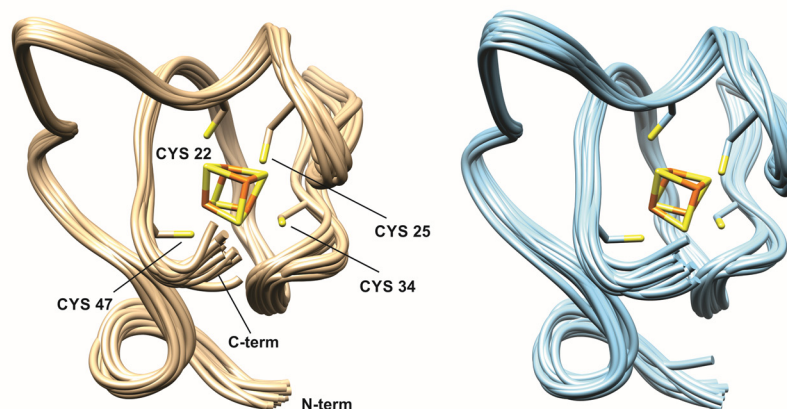
Figure 4. NMR structures of PioC obtained with full set of restraints (beige) and ^{13}C PRE restrains less structure (cyan). Residues 5–49 are shown.
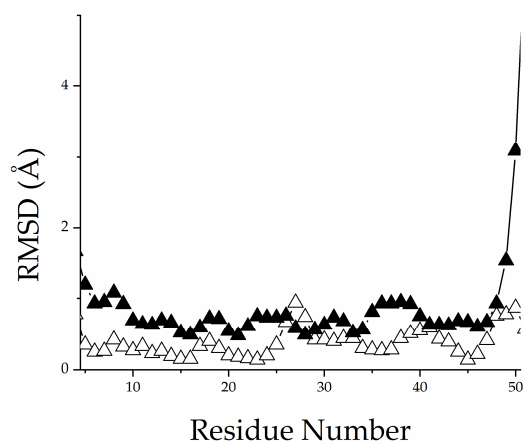
Figure 5. Per-residue backbone RMSD (5–50). The RMSD between the two mean structures (white triangles) is compared with the sum of the pairwise backbone RMSD of each ensemble (black triangles).
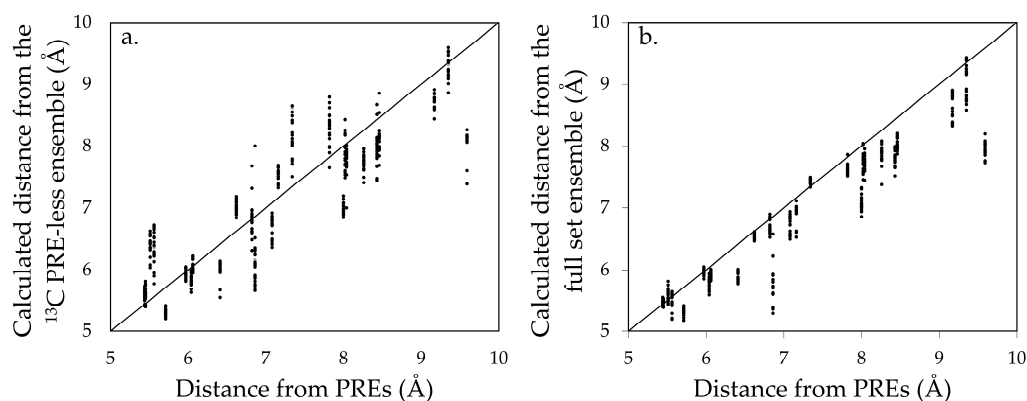

Figure 6. PRE-derived distances vs. solution structures distances. The structures have been calculated without the ^{13}C PRE restraints (**a**) and using the full set of restraints (**b**). In the 5–9 Å distance range, the dispersion of calculated distances from the structures are significantly decreased. When ^{13}C PREs are used to refine the structure (**b**) the calculated distances are restrained with a very few violations observed in the b. part of the figure (values above the line representing the upl values).

4. Conclusions

We have shown here that ^{13}C PRE-based restraints provide a consistent set of NMR restraints that can be added to ^{1}H PREs and to other classical and paramagnetism-based NMR restraints, to improve quality and quantity of the NMR information. The range of distances sampled by ^{13}C PREs, within each paramagnetic center, is different from that of ^{1}H PREs, therefore the consistency between the two sets of data it is not straightforward and needs to be verified and assessed. The synergistic effect of ^{13}C and ^{1}H PREs restraints, that we have demonstrated in PioC as a proof of concept, will be even more beneficial for systems in which the paramagnetic effects are stronger. In those cases, the combined use of ^{13}C and ^{1}H PREs restraints will then be mandatory to reduce the blind sphere around the metal and improve calculation precision and accuracy. It is well known that the redundancy of NOEs is important to obtain accurate NMR solution structures [56–58]; this study shows that this also holds for PREs. This widens up the interest for measuring an increased number of relaxation rates. Small metalloproteins like PioC represent a paradigmatic case to assess the effect of PREs. This can be extremely useful for the NMR characterization of native metalloproteins where the metal center cannot be substituted, *denovo* designed metalloproteins [59], metalloproteins in which the metal center can be replaced with a paramagnetic probe [60,61], paramagnetic proteins of larger size and complexity [62–64], and in diamagnetic proteins where the use of metal tags may contribute to elucidate protein–

protein interactions [16,65]. Finally, it is worth mentioning that ^{13}C detected NMR is also a robust approach to study high molecular weight systems such as large size proteins, protein–protein complexes and antibodies [66].

Author Contributions: Conceptualization: F.C., R.O.L. and M.P.; Investigation: L.Q., I.B.T., J.M.S. and M.I.; Writing—Original Draft preparation: L.Q., J.M.S. and M.P.; Writing—Review and Editing: L.Q., I.B.T., J.M.S., M.I., F.C., R.O.L. and M.P.; Supervision: F.C., R.O.L. and M.P. All authors have read and agreed to the published version of the manuscript.

Institutional Review Board Statement: Not applicable.

Informed Consent Statement: Not applicable.

Conflicts of Interest: The authors declare no conflict of interest.

References

1. Banci, L.; Camponeschi, F.; Ciofi-Baffoni, S.; Piccioli, M. The NMR contribution to protein-protein networking in Fe-S protein maturation. *J. Biol. Inorg. Chem.* **2018**, *23*, 665–685. [CrossRef]
2. Piccioli, M.; Turano, P. Transient iron coordination sites in proteins: Exploiting the dual nature of paramagnetic NMR. *Coord. Chem. Rev.* **2015**, *284*, 313–328. [CrossRef]
3. Piccioli, M. Paramagnetic NMR Spectroscopy Is a Tool to Address Reactivity, Structure, and Protein-Protein Interactions of Metalloproteins: The Case of Iron-Sulfur Proteins. *Magnetochemistry* **2020**, *6*, 46. [CrossRef]
4. Trindade, I.B.; Coelho, A.; Cantini, F.; Piccioli, M.; Louro, R.O. NMR of paramagnetic metalloproteins in solution: Ubi venire, quo vadis? *J. Inorg. Biochem.* **2022**, *234*, 111871. [CrossRef]
5. Clore, G.M. Practical Aspects of Paramagnetic Relaxation Enhancement in Biological Macromolecules. *Methods Enzymol.* **2015**, *564*, 485–497.
6. Hus, J.C.; Marion, D.; Blackledge, M. De novo determination of protein structure by NMR using orientational and long-range order restraints. *J. Mol. Biol.* **2000**, *298*, 927–936. [CrossRef]
7. Ramelot, T.A.; Cort, J.R.; Goldsmith-Fischman, S.; Kornhaber, G.J.; Xiao, R.; Shastry, R.; Acton, T.B.; Honig, B.; Montelione, G.T.; Kennedy, M.A. Solution NMR structure of the iron-sulfur cluster assembly protein U (IscU) with zinc bound at the active site. *J. Mol. Biol.* **2004**, *344*, 567–583. [CrossRef] [PubMed]
8. Parigi, G.; Ravera, E.; Luchinat, C. Paramagnetic effects in NMR for protein structures and ensembles: Studies of metalloproteins. *Curr. Opin. Struct. Biol.* **2022**, *74*, 102386. [CrossRef]
9. Swartjes, A.; White, P.B.; Bruekers, J.P.J.; Elemans, J.A.A.W.; Nolte, R.J.M. Paramagnetic relaxation enhancement NMR as a tool to probe guest binding and exchange in metallohosts. *Nat. Commun.* **2022**, *13*, 1846. [CrossRef]
10. Karschin, N.; Becker, S.; Griesinger, C. Interdomain Dynamics via Paramagnetic NMR on the Highly Flexible Complex Calmodulin/Munc13-1. *J. Am. Chem. Soc.* **2022**, *144*, 17041–17053. [CrossRef]
11. Pell, A.J.; Pintacuda, G.; Grey, C.P. Paramagnetic NMR in solution and the solid state. *Prog. Nucl. Magn. Reson. Spectrosc.* **2019**, *111*, 1–271. [CrossRef]
12. Pan, B.B.; Yang, F.; Ye, Y.; Wu, Q.; Li, C.; Huber, T.; Su, X.C. 3D structure determination of a protein in living cells using paramagnetic NMR spectroscopy. *Chem. Commun.* **2016**, *52*, 10237–10240. [CrossRef]
13. Donaldson, L.W.; Skrynnikov, N.R.; Choy, W.Y.; Muhandiram, D.R.; Sarkar, B.; Forman-Kay, J.D.; Kay, L.E. Structural characterization of proteins with an attached ATCUN motif by paramagnetic relaxation enhancement NMR spectroscopy. *J. Am. Chem. Soc.* **2001**, *123*, 9843–9847. [CrossRef]
14. Rumpel, S.; Ravera, E.; Sommer, C.; Reijerse, E.J.; Fares, C.; Luchinat, C.; Lubitz, W. ^{1}H NMR spectroscopy of (FeFe) hydrogenase: Insight into the electronic structure of the active site. *J. Am. Chem. Soc.* **2018**, *140*, 131–134. [CrossRef]
15. Joss, D.; Haussinger, D. Design and applications of lanthanide chelating tags for pseudocontact shift NMR spectroscopy with biomacromolecules. *Prog. Nucl. Magn. Reson. Spectrosc.* **2019**, *114–115*, 284–312. [CrossRef]
16. Miao, Q.; Nitsche, C.; Orton, H.; Overhand, M.; Otting, G.; Ubbink, M. Paramagnetic Chemical Probes for Studying Biological Macromolecules. *Chem. Rev.* **2022**, *122*, 9571–9642. [CrossRef] [PubMed]
17. Orton, H.W.; Otting, G. Accurate Electron–Nucleus Distances from Paramagnetic Relaxation Enhancements. *J. Am. Chem. Soc.* **2018**, *140*, 7688–7697. [CrossRef] [PubMed]

18. Toyama, Y.; Rangadurai, A.K.; Kay, L.E. Measurement of $^1H^\alpha$ transverse relaxation rates in proteins: Application to solvent PREs. *J. Biomol. NMR* **2022**, *76*, 137–152. [CrossRef] [PubMed]

19. Lenard, A.J.; Mulder, F.A.A.; Madl, T. Solvent paramagnetic relaxation enhancement as a versatile method for studying structure and dynamics of biomolecular systems. *Prog. Nucl. Magn. Reson. Spectrosc.* **2022**, *132–133*, 113–139. [CrossRef]

20. Ravera, E.; Gigli, L.; Fiorucci, L.; Luchinat, C.; Parigi, G. The evolution of paramagnetic NMR as a tool in structural biology. *Phys. Chem. Chem. Phys.* **2022**, *24*, 17397–17416. [CrossRef]

21. Parker, D.; Suturina, E.A.; Kuprov, I.; Chilton, N.F. How the Ligand Field in Lanthanide Coordination Complexes Determines Magnetic Susceptibility Anisotropy, Paramagnetic NMR Shift, and Relaxation Behavior. *Acc. Chem. Res.* **2020**, *53*, 1520–1534. [CrossRef]

22. Vogel, R.; Müntener, T.; Häussinger, D. Intrinsic anisotropy parameters of a series of lanthanoid complexes deliver new insights into the structure-magnetism relationship. *Chem* **2021**, *7*, 3144–3156. [CrossRef]

23. Abelein, A.; Ciofi-Baffoni, S.; Mörman, C.; Kumar, R.; Giachetti, A.; Piccioli, M.; Biverstål, H. Molecular Structure of Cu(II)-Bound Amyloid-β Monomer Implicated in Inhibition of Peptide Self-Assembly in Alzheimer's Disease. *JACS Au* **2022**, *2*, 2571–2584. [CrossRef]

24. Trindade, I.B.; Invernici, M.; Cantini, F.; Louro, R.O.; Piccioli, M. PRE-driven protein NMR structures: An alternative approach in highly paramagnetic systems. *FEBS J.* **2021**, *288*, 3010–3023. [CrossRef] [PubMed]

25. Bird, L.J.; Saraiva, I.H.; Park, S.; Calcada, E.O.; Salgueiro, C.A.; Nitschke, W.; Louro, R.O.; Newman, D.K. Nonredundant roles for cytochrome c_2 and two high-potential iron-sulfur proteins in the photoferrotroph *Rhodopseudomonas palustris* TIE-1. *J. Bacteriol.* **2014**, *196*, 850–858. [CrossRef] [PubMed]

26. Invernici, M.; Trindade, I.B.; Cantini, F.; Louro, R.O.; Piccioli, M. Measuring transverse relaxation in highly paramagnetic systems. *J. Biomol. NMR* **2020**, *74*, 431–442. [CrossRef]

27. Ciofi-Baffoni, S.; Gallo, A.; Muzzioli, R.; Piccioli, M. The IR-^{15}N-HSQC-AP experiment: A new tool for NMR spectroscopy of paramagnetic molecules. *J. Biomol. NMR* **2014**, *58*, 123–128. [CrossRef]

28. Arnesano, F.; Banci, L.; Piccioli, M. NMR structures of paramagnetic metalloproteins. *Q. Rev. Biophys.* **2005**, *38*, 167–219. [CrossRef] [PubMed]

29. Trindade, I.B.; Hernandez, G.; Lebegue, E.; Barriere, F.; Cordeiro, T.; Piccioli, M.; Louro, R.O. Conjuring up a ghost: Structural and functional characterization of FhuF, a ferric siderophore reductase from *E. coli*. *J. Biol. Inorg. Chem.* **2021**, *26*, 313–326. [CrossRef]

30. Arnesano, F.; Banci, L.; Bertini, I.; Felli, I.C.; Luchinat, C.; Thompsett, A.R. A strategy for the NMR characterization of type II copper(II) proteins: The case of the copper trafficking protein CopC from *Pseudomonas syringae*. *J. Am. Chem. Soc.* **2003**, *125*, 7200–7208. [CrossRef]

31. Piccioli, M.; Poggi, L. Tailored HCCH-TOCSY experiment for resonance assignment in the proximity of a paramagnetic center. *J. Magn. Reson.* **2002**, *155*, 236–243. [CrossRef] [PubMed]

32. Alik, A.; Bouguechtouli, C.; Julien, M.; Bermel, W.; Ghouil, R.; Zinn-Justin, S.; Theillet, F.X. Sensitivity-Enhanced 13 C-NMR Spectroscopy for Monitoring Multisite Phosphorylation at Physiological Temperature and pH. *Angew. Chem. Int. Ed.* **2020**, *59*, 10411–10415. [CrossRef]

33. Cerofolini, L.; Staderini, T.; Giuntini, S.; Ravera, E.; Fragai, M.; Parigi, G.; Pierattelli, R.; Luchinat, C. Long-range paramagnetic NMR data can provide a closer look on metal coordination in metalloproteins. *J. Biol. Inorg. Chem.* **2018**, *23*, 71–80. [CrossRef]

34. Bermel, W.; Bertini, I.; Felli, I.; Piccioli, M.; Pierattelli, R. 13C-detected protonless NMR spectroscopy of proteins in solution. *Prog. Nucl. Magn. Reson. Spectrosc.* **2006**, *48*, 25–45. [CrossRef]

35. Caillet-Saguy, C.; Delepierre, M.; Lecroisey, A.; Bertini, I.; Piccioli, M.; Turano, P. Direct detected ^{13}C NMR to investigate the Iron(III) hemophore HasA. *J. Am. Chem. Soc.* **2006**, *128*, 150–158. [CrossRef]

36. Felli, I.C.; Pierattelli, R. ^{13}C Direct Detected NMR for Challenging Systems. *Chem. Rev.* **2022**, *122*, 9468–9496. [CrossRef]

37. Trindade, I.B.; Invernici, M.; Cantini, F.; Louro, R.O.; Piccioli, M. ^{1}H, ^{13}C and ^{15}N assignment of the paramagnetic high potential iron–sulfur protein (HiPIP) PioC from *Rhodopseudomonas palustris* TIE-1. *Biomol. NMR Assign.* **2020**, *14*, 211–215. [CrossRef]

38. Pontoriero, L.; Schiavina, M.; Murrali, M.G.; Pierattelli, R.; Felli, I.C. Monitoring the Interaction of α-Synuclein with Calcium Ions through Exclusively Heteronuclear Nuclear Magnetic Resonance Experiments. *Angew. Chem. Int. Ed.* **2020**, *59*, 18537–18545. [CrossRef]

39. Emsley, L.; Bodenhausen, G. Optimization of shaped selective pulses for NMR using a quaternion description of their overall propagators. *J. Magn. Reason.* **1992**, *97*, 135–148. [CrossRef]

40. Keller, R. *The Computer Aided Resonance Assignment Tutorial*; CANTINA Verlag: Goldau, Switzerland, 2004; 81p.

41. Güntert, P. Automated NMR structure calculation with CYANA. *Methods Mol. Biol.* **2004**, *278*, 353–378.

42. Guntert, P.; Buchner, L. Combined automated NOE assignment and structure calculation with CYANA. *J. Biomol. NMR* **2015**, *62*, 453–471. [CrossRef]

43. Dutta, S.K.; Serrano, P.; Proudfoot, A.; Geralt, M.; Pedrini, B.; Herrmann, T.; Wthrich, K. APSY-NMR for protein backbone assignment in high-throughput structural biology. *J. Biomol. NMR* **2015**, *61*, 47–53. [CrossRef] [PubMed]

44. Zeng, L.; Fischer, M.W.F.; Zuiderweg, E.R.P. Study of protein dynamics in solution by measurement of $^{13}C^\alpha$-^{13}CO NOE and ^{13}CO longitudinal relaxation. *J. Biomol. NMR* **1996**, *7*, 157–162. [CrossRef]

45. Bermel, W.; Bertini, I.; Felli, I.C.; Peruzzini, R.; Pierattelli, R. Exclusively heteronuclear NMR experiments to obtain structural and dynamic information on proteins. *ChemPhysChem* **2010**, *11*, 689–695. [CrossRef]

46. Camponeschi, F.; Gallo, A.; Piccioli, M.; Banci, L. The long-standing relationship between Paramagnetic NMR and Iron-Sulfur proteins: The mitoNEET example. An old method for new stories or the other way around? *Magn. Reson. Discuss.* **2021**, *2*, 203–211. [CrossRef]

47. Grifagni, D.; Silva, J.M.; Cantini, F.; Piccioli, M.; Banci, L. Relaxation-based NMR assignment: Spotlights on ligand binding sites in human CISD3. *J. Inorg. Biochem.* **2023**, *239*, 112089. [CrossRef]

48. Bertini, I.; Jimenez, B.; Piccioli, M. [13]C direct detected experiments: Optimization for paramagnetic signals. *J. Magn. Reson.* **2005**, *174*, 125–132. [CrossRef]

49. Trindade, I.B.; Invernici, M.; Cantini, F.; Louro, R.O.; Piccioli, M. Sequence-specific assignments in NMR spectra of paramagnetic systems: A non-systematic approach. *Inorg. Chim. Acta* **2021**, *514*, 119984. [CrossRef]

50. Bertini, I.; Capozzi, F.; Luchinat, C.; Piccioli, M.; Vicens Oliver, M. NMR is a unique and necessary step in the investigation of iron-sulfur proteins: The HiPIP from *R. gelatinosus* as an example. *Inorg. Chim. Acta* **1992**, *198–200*, 483–491. [CrossRef]

51. Bertini, I.; Luchinat, C.; Parigi, G.; Ravera, E. *NMR of Paramagnetic Molecules*; Elsevier: Amsterdam, The Netherlands, 2017; 508p.

52. Banci, L.; Bertini, I.; Luchinat, C.; Piccioli, M.; Scozzafava, A.; Turano, P. [1]H NOE studies on dicopper(II) dicobalt(II) superoxide dismutase. *Inorg. Chem.* **1989**, *28*, 4650–4656. [CrossRef]

53. Spronk, C.; Zerko, S.; Gorka, M.; Kozminski, W.; Bardiaux, B.; Zambelli, B.; Musiani, F.; Piccioli, M.; Basak, P.; Blum, F.C.; et al. Structure and dynamics of Helicobacter pylori nickel-chaperone HypA: An integrated approach using NMR spectroscopy, functional assays and computational tools. *J. Biol. Inorg. Chem.* **2018**, *23*, 1309–1330. [CrossRef]

54. Bertini, I.; Capozzi, F.; Luchinat, C.; Piccioli, M.; Vila, A.J. The Fe_4S_4 centers in ferredoxins studied through proton and carbon hyperfine coupling. Sequence specific assignments of cysteines in ferredoxins from *Clostridium acidi urici* and *Clostridium pasteurianum*. *J. Am. Chem. Soc.* **1994**, *116*, 651–660. [CrossRef]

55. Banci, L.; Bertini, I.; Cantini, F.; Della Malva, N.; Rosato, A.; Herrmann, T.; Wüthrich, K. Solution structure and intermolecular interactions of the third metal-binding domain of ATP7A, the Menkes disease protein. *J. Biol. Chem.* **2006**, *281*, 29141–29147. [CrossRef] [PubMed]

56. Sala, D.; Huang, Y.J.; Cole, C.A.; Snyder, D.A.; Liu, G.; Ishida, Y.; Swapna, G.V.T.; Brock, K.P.; Sander, C.; Fidelis, K.; et al. Protein structure prediction assisted with sparse NMR data in CASP13. *Proteins* **2019**, *87*, 1315–1332. [CrossRef]

57. Duclert-Savatier, N.; Martínez, L.; Nilges, M.; Malliavin, T.E. The redundancy of NMR restraints can be used to accelerate the unfolding behavior of an SH3 domain during molecular dynamics simulations. *BMC Struct. Biol.* **2011**, *11*, 46. [CrossRef]

58. Nabuurs, S.B.; Spronk, C.A.; Krieger, E.; Maassen, H.; Vriend, G.; Vuister, G.W. Quantitative evaluation of experimental NMR restraints. *J. Am. Chem. Soc.* **2003**, *125*, 12026–12034. [CrossRef]

59. Kim, J.D.; Pike, D.H.; Tyryshkin, A.M.; Swapna, G.V.T.; Raanan, H.; Montelione, G.T.; Nanda, V.; Falkowski, P.G. Minimal Heterochiral de Novo Designed 4Fe-4S Binding Peptide Capable of Robust Electron Transfer. *J. Am. Chem. Soc.* **2018**, *140*, 11210–11213. [CrossRef] [PubMed]

60. Balayssac, S.; Jiménez, B.; Piccioli, M. Assignment Strategy for Fast Relaxing Signals: Complete Aminoacid Identification in Thulium Substituted Calbindin D_{9k}. *J. Biomol. NMR* **2006**, *34*, 63–73. [CrossRef]

61. Invernici, M.; Selvolini, G.; Silva, J.M.; Marrazza, G.; Ciofi-Baffoni, S.; Piccioli, M. Interconversion between [2Fe-2S] and [4Fe-4S] cluster glutathione complexes. *Chem. Commun.* **2022**, *58*, 3533–3536. [CrossRef] [PubMed]

62. Okuno, Y.; Schwieters, C.D.; Yang, Z.; Clore, G.M. Theory and Applications of Nitroxide-based Paramagnetic Cosolutes for Probing Intermolecular and Electrostatic Interactions on Protein Surfaces. *J. Am. Chem. Soc.* **2022**, *144*, 21371–21388. [CrossRef] [PubMed]

63. Arthanari, H.; Takeuchi, K.; Dubey, A.; Wagner, G. Emerging solution NMR methods to illuminate the structural and dynamic properties of proteins. *Curr. Opin. Struct. Biol.* **2019**, *58*, 294–304. [CrossRef] [PubMed]

64. Bax, A.; Clore, G.M. Protein NMR: Boundless opportunities. *J. Magn. Reson.* **2019**, *306*, 187–191. [CrossRef] [PubMed]

65. Deshmukh, L.; Louis, J.M.; Ghirlando, R.; Clore, G.M. Transient HIV-1 Gag-protease interactions revealed by paramagnetic NMR suggest origins of compensatory drug resistance mutations. *Proc. Natl. Acad. Sci. USA* **2016**, *113*, 12456–12461. [CrossRef] [PubMed]

66. Arbogast, L.W.; Brinson, R.G.; Marino, J.P. Mapping Monoclonal Antibody Structure by 2D ^{13}C NMR at Natural Abundance. *Anal. Chem.* **2015**, *87*, 3556–3561. [CrossRef]